Observing Planets and Small Bodies in Sputtered High Energy Atom (SHEA) Fluxes

A. Milillo[1], S. Orsini[1], K. C. Hsieh[2], R. Baragiola[3], M. Fama[3], R. Johnson[3], A. Mura[1], Ch. Plainaki[1], M. Sarantos[4], T. A. Cassidy[5], E. De Angelis[1], M. Desai[6], R. Goldstein[6], W.-H. Ip[7], R. Killen[8], S. Livi[6]

(1) INAF/IFSI, via del Fosso del Cavaliere, 00133 Roma, Italy.

(2) Department of Physics, University of Arizona, Tucson, AZ 85721, U.S.A.

(3) Materials Science and Engineering, University of Virginia, Charlottesville, VA 22904, U.S.A.

(4) Heliophysics Division, NASA GSFC, Code 670.0, Greenbelt, MD 20771, U.S.A.

(5) Jet Propulsion Laboratory, M/S 183-601, Pasadena, CA 91109, U.S.A.

(6) Southwest Research Institute, P.O. Drawer 28510, San Antonio, TX 78228, U.S.A.

(7) Department of Astronomy, National Central University, Jhongli, Taiwan 32001, R.O.C.

(8) Planetary Magnetospheres Division, NASA GSFC, Code 695.0, Greenbelt, MD 20771, U.S.A.

Abstract. The evolution of the surfaces of bodies unprotected by either strong magnetic fields or thick atmospheres in the Solar System is caused by various processes, induced by photons, energetic ions and micrometeoroids. Among these processes, the continuous bombardment of the solar wind or energetic magnetospheric ions onto the bodies may significantly affect their surfaces, with implications for their evolution. Ion precipitation produces neutral atom releases into the exosphere through ion sputtering, with velocity distribution extending well above the particle escape limits. We refer to this component of the surface ejecta as *sputtered high-energy atoms* (SHEA). The use of ion sputtering emission for studying the interaction of *exposed bodies* (EB) with ion environments is described here. Remote sensing in SHEA in the vicinity of EB can provide mapping of the bodies exposed to ion sputtering action with temporal and mass resolution. This paper speculates on the possibility of performing remote sensing of exposed bodies using SHEA

and suggests the need for quantitative results from laboratory simulations and molecular physic modeling in order to understand SHEA data from planetary missions. In the Appendix, referenced computer simulations using existing sputtering data are reviewed.

1. Introduction

Studying the evolution of the surfaces and atmospheres of bodies in the Solar System is fundamental to our understanding of the present composition of planetary surfaces and atmospheres. This endeavor entails finding how the rates of the on-going processes vary as a function of the space environment. Aside from occasional catastrophic events, such as volcanic eruptions in a few bodies or occasional collisions with comets and asteroids, surface and atmospheric changes are caused predominantly by the continuous bombardment of the bodies by photons, energetic ions and micrometeoroids. Yet the actual effects of these incident fluxes on the present state of planetary bodies are not well described. To investigate this complex topic, we propose to begin with a much simpler quest by focusing on the subset of planets, moons and small bodies that are not protected by either strong magnetic fields or thick atmospheres. For surfaces of exposed bodies (EB) such as Mercury, Moon, and asteroids, directly exposed to the solar wind, the alteration of the solid surface and the production of the surface-bound exospheres by the impacts of the time-varying solar wind (SW) over the last 4.54 Gy constitute a relevant component of space weathering. For other EB, such as Callisto, Europa and Ganymede of Jupiter, energetic magnetospheric (MS) ions play the major role in altering the respective surfaces and atmospheres. Hence, we shall focus on the process of ion sputtering (IS) on EB, *i.e.* on bombardment by either SW or MS ions.

In the past, the nature of space weathering has been reviewed in detail and the sputter alteration of regoliths of outer solar system bodies has been discussed (Hapke, 1986; 2001). Moreover, a mathematical theory describing the optical effects of space weathering has been derived and applied to the regoliths of the Moon, Mercury and an S asteroid (Hapke, 2001). Whereas Hapke (2001) discussed the spectral effects and the melting of minerals caused by space weathering, in this study

54 we consider as its main specific signature the flux of energetic atoms ejected upon impact of
55 energetic particles on the surfaces.
56 Although there are other surface-ejected atoms and molecules, such as those released by thermal
57 desorption (TD), photon-stimulated desorption (PSD) and micrometeoroid impact vaporization
58 (MIV), we shall show that IS ejecta produced by the incident SW or MS ions provide a unique
59 window to observe space weathering of EB. These ions may be partly neutralized and back-
60 scattered from the surface to space (up to 20% for light ions like the SW major components, see
61 McComas et al., 2009, and Wieser et al., 2009), but a significant fraction of the incident ions,
62 increasing with ions atomic mass number, can be implanted on the EB surface while ejecting a
63 surface atom or molecule. Sputtering products from impacts of keV ions can have energies, peaking
64 at few eV with a high-energy non-Maxwellian tail, up to at least several tens eV for a refractory
65 material (Goelhich et al. 2000). We refer to this component of the surface ejecta as *sputtered high-*
66 *energy atoms* (SHEA). At these energies, SHEA emitted from regolith can easily escape the local
67 gravity (*e.g.*, 0.09 eV/nucleon for Mercury and 0.03 eV/nucleon for the Moon) and be distinguished
68 from other surface-released products from TD, PSD and MIV, all typically $\leq$1 eV. Plainaki et al.
69 (2010) show that even in the case of icy moons the flux of escaping IS ejectia is significantly higher
70 than the other products (see also Figure A5 in the Appendix). The energy spectra of SHEA, of
71 course, strongly depend on the incident flux and surface composition. Being electrically neutral and
72 energetic, SHEA can escape both the magnetic and gravitational field present between their places
73 of birth (where sputtering occurs) and a SHEA analyzer onboard either an orbiter or a fly-by probe.
74 If, on the same spacecraft, the SW or MS ions are monitored by a plasma analyzer and the surface
75 composition of the *exposed bodies* (EB) analyzed by IR, X-ray, γ-ray or neutron spectrometers, then
76 the detection of mass and energy distributions of SHEA would provide the missing piece in
77 determining the magnitude and rate of space weathering of the given EB's surface as well as the
78 composition of its surface-bound exosphere.

79 Recent observations of heavy pickup ions at Mercury by the MESSENGER spacecraft (Zurbuchen
80 *et al.*, 2008) and the pickup ions from reflected SW protons at the Moon by the *Kaguya* spacecraft
81 (Saito *et al.*, 2008) have shown most clearly that SW-ion and EB-surface interactions are a link
82 between the physics of space plasma and of surface-bound exospheres. Furthermore, Chandrayaan-
83 1 Energetic Neutrals Analyzer (CENA) was, in principle, able to measure neutral atoms of 10 eV to
84 3 keV (Bhardwaj et al., 2005). This sensor observed an energetic neutral signal from the Moon
85 surface, interpreted as the product of neutralization and back-scattering of the solar wind, probably
86 prevailing on sputtering signal at the Moon (Wieser et al. 2009). The results and sensitivity of
87 CENA could provide an indication for estimating an upper limit of the flux of SHEA around the
88 Moon. These recent results come, however, from in-situ measurements of the already processed
89 surface releases. Were *remote sensing of the surface via SHEA* from the vicinity of Mercury and of
90 Moon with appropriate instrumentation available, then more direct and detailed investigations could
91 be done on the nature of the surface-plasma interaction under different physical conditions, *e.g.*, SW
92 condition, solar radiation effect, magnetospheric condition, and surface property. Such
93 investigations may be carried-on by monitoring SHEA flux intensity, emitting area extension and
94 particle relative abundances. The comparison between the ground-based observations and
95 spacecraft measurements and between pickup-ion and SHEA measurements would resolve many
96 outstanding issues such as the interplay between ion-sputtering and photo-desorption by solar UV
97 photons, the relative importance of thermal desorption and meteoroid impact as source mechanisms
98 of the sputtered exospheric atoms.
99 Clearly, to accurately interpret any SHEA data from space weathering effects on surfaces of EB will
100 require active participation of physicists doing sputtering experiments in laboratories directly
101 applicable to the interactions between SW or MS ions and EB surfaces. Only such experiments can
102 quantify the microscopic processes controlling the sputtering yield Y_i, the number of released
103 particles per incident ion, basic to remote sensing in SHEA.

Remote sensing EB *via* SHEA by orbiters or fly-by probes can also provide information to complement the observations from Earth or by instruments landed on these solid bodies. Although fly-by missions offer only brief observation of one body, each mission could be planned to fly by several bodies. The advantage of orbiters over landers, besides cost, is its global survey under varying conditions over longer time periods. In the case of orbiting larger planets with many moons, the ability to observe several moons has been successfully demonstrated by missions *Galileo* and *Cassini*. These and other orbiter missions, unfortunately, are not equipped to study space weathering of the EB. To examine the issue of SHEA capability on future EB missions, an in-depth discussion is necessary.

To begin this discussion, we start with the data and techniques currently available to assess whether or not SHEA instruments are critical to future orbiter or fly-by missions. To this end, details are presented in the following manner: the production of SHEA in §2, justification for SHEA observation in §3, the need for laboratory-based ground truth in sputtering in §4, and the conclusions in §5. Examples of computer simulations of SHEA emissions from Mercury, Moon, asteroids and Jovian Moons, based on existing data and theories, are presented in the Appendix.

2. Production of SHEA

The IS results from the impact of an ion of mass m_1 onto a solid surface. If the ion incident energy E_i is high enough, surface atoms may be ejected. Some IS processes producing SHEA are represented in Figure 1. For oblique incidence, ion sputtering can be a single-step process, often called "knock-on", in which the ions directly eject surface atoms (a). Otherwise, a multi-step process takes place, often called "collision cascade" (d). Light incident ions are often backscattered in layers near the surface, and occasionally they may be neutralized in the process before returning to space – not shown, but would be like in (e) without the second collision. Backscattered ions can trigger a cascade of collisions among atoms close to the surface. While the heavy incident ions produce forward-directed recoils.

130 The energy transferred in the first collision to a surface atom is given by classical mechanics:

131
$$T = T_m \cos^2 \alpha_r$$
$$T_m = E_i \frac{4\, m_1 m_2}{(m_1 + m_2)^2} \quad (1)$$

132 where E_i and m_1 are the incident ion energy and mass, respectively, m_2 is the mass of the struck
133 atom (the recoil), T the energy transfer, T_m its maximum value, and α_r the scattering angle of the
134 recoil atom (see Figure 1). Collisions below the surface layer involve both the projectile and the
135 recoil atoms, with the cascade of collisions eventually leading to sputtering, i.e. the ejection of an
136 atom or molecule from the solid. For a regolith material (independently of composition or porosity),
137 the ejected particles are mostly neutral atoms (Hofer, 1991). For ejected atoms or molecules of
138 species n with partial sputtering yield Y_n, the normalized distribution of ejecta ($f_{S,n}$) from a
139 refractory material, as a function of ejecta energy E_e, can peak at few eV (Gnaser 2007; Hofer 1991)
140 and can often be empirically reproduced by the following function (Sigmund, 1969; Sieveka and
141 Johnson, 1984):

142
$$f_{S,n}(E_e, E_i, \alpha_n) = c_n \frac{E_e}{(E_e + E_{b,n})^3} \left[1 - \sqrt{\frac{E_e + E_{b,n}}{T_m}}\right] \cos\alpha_n \quad (2)$$

143 where $E_{b,n}$ is the surface binding energy of the ejected atoms, α_n the polar angle of the SHEA with
144 respect to the surface normal (Figure 1), and c_n the normalization constant. Gnaser (2007) showed
145 that the effective binding energy $E_{b,n}$ is typically lower than the bulk cohesive energy. For
146 refractory materials, the difference between the two can be as much as 50%, but more typically ~
147 10-20%. For volatile materials that dominate the outer solar system, the difference can be an order
148 of magnitude (e.g., Reimann et al. 1984; Johnson et al. 2010). Empirically, all variables in Eq. (2)
149 can be measured, except $E_{b,n}$. By fitting Eq. (2) to laboratory data on sputtering, therefore, can
150 uniquely determine $E_{b,n}$.

151 Samples for comparing computed with measured $f_{S,n}$ as functions of E_e for different incident ions
152 and solid targets are shown in Figure 2. Panels (a) and (b) are $f_{S,n}$ computed for Na ejected by

153 protons incident on a planetary-like mineral for different values of $E_{b,Na}$ and of E_i, respectively,
154 using Eq. (2) averaged over angle α_n (Sigmund, 1969; Sieveka and Johnson, 1984). It is clear that
155 E_i sets the upper limit on E_e, while E_b affects the energy at which the distribution peaks. Panel (c)
156 shows good agreement between Monte Carlo SRIM (Ziegler et al., 1966) simulation results (for a
157 surface composition derived by Goettel, 1988) and Eq. (2) in the high-energy tail in the case of 1-
158 keV protons on a planetary-like surface. Moreover, panel (d) compares Eq. (2) with experimental
159 results of Ar^+ impacting on W at four different values of E_i for $\theta_i = \alpha_n = 0$ (Figure 3 of Goelhich et
160 al., 2000) with Eq. (2); the agreement improves for $E_i > 500$ eV. The spectrum of the ejected Na
161 shown in panel (e) is converted from velocity to energy E_e as the independent variable, resulting
162 from bombarding a Na_2SO_4 target with 3.5-keV Ar^+, as might be the case for surfaces of Io (Wiens
163 et al. 1997) or, possibly, certain regions of Europa although Na is often in an ice matrix (e.g.,
164 Johnson et al. 2002). The spectrum fits the form of Eq. (2), which has a measured tail extending to a
165 few eV, but peaks at ~ 0.3 eV, well below that shown in panel (d). They also showed that the
166 Monte Carlo SRIM is able as well to reproduce the process for different impact energies and angles.
167 Panel (f) gives the energy spectra of sputtered D_2O and SO_2 from 5-keV Ar^+ impacting a heavy-
168 water ice matrix containing SO_2 (Johnson et al., 2010). Figure 2 demonstrates the wide
169 applicability of Eq. (2), except for the lowest energy portion showed in panel (f), as explained in
170 Johnson et al. (2010), and the need to establish $E_{b,n}$ for incident ions and targets relevant to the
171 study of space weathering of selected EB.
172 The angular distribution of the ejected atoms depends on the incident ion mass so that a general
173 expression is not easily defined; detailed discussions can be found in Hofer (1991) and Gnaser
174 (2007). For heavy incident ions, the ion impact direction does not have a large effect on the
175 distribution in ejection angle α_n, which is often approximated $\cos^k(\alpha_n)$, where k is usually between
176 1, as in Eq. (2), and 2. For light ions, the angular distribution is related to the ion impact direction,
177 and exhibits a maximum close to the mirroring angle. For a surface composed of a number of
178 different atomic species, the angle-averaged differential flux of sputtered atoms is:

179 $$\frac{d\Phi}{dE_e} = \sum_n C_n \int_{E_{min}}^{E_{max}} \frac{d\Phi_I}{dE_i} Y_n f_{s,n}(E_e, E_i) dE_i, \quad (3)$$

180 where C_n is the relative surface abundance of the atomic species n, and Φ_I is the incident ion flux.
181 The total sputtering yield $Y=\int(d\Phi/dE_e)dE_e$, in general, depends on the impinging ion mass and
182 energy and on the surface mineralogy. Averaged over the solar-wind ion energies, Y can range from
183 0.01 – 0.1 (Lammer *et al.*, 2003; Johnson and Baragiola 1991) for refractory surfaces, whereas it
184 ranges in between 10 – 1000 for icy surfaces of the Jovian moons when bombarded by hundreds
185 keV MS heavy ions (Johnson 1990; Famá et al. 2008; Johnson et al. 2010). These values are
186 reduced by the regolith porosity (Cassidy and Johnson, 2005). The yield is also a function of the
187 incident ion's mass and nuclear charge. In general, every precipitating ion contributes to sputtering
188 from the EB surface. For example, accounting for the solar wind abundance of the ions, the net
189 sputtering rate generated by protons with respect to other solar-wind components, like α particles or
190 high-charge-state particles, is estimated to be comparable (Johnson and Baragiola, 1991). In the
191 case of the icy moons of the giant planets hit by heavy and energetic magnetospheric plasma ions,
192 the ejecta are dominated by low-energy atoms and molecules. Since the yields from such surfaces
193 can be large, both simulations (Cassidy et al. 2009) and experiments (Johnson et al. 2010) show that
194 the trace species are carried off with the ice matrix. The two sets of EB, one exposed to SW only
195 and the other exposed predominantly to magnetospheric plasma, make a comparative study that
196 would improve our understanding of the mechanism of space weathering.
197

198 ## 3. The uniqueness of SHEA observation

199 *3.1 Selecting a starting point in the study of surface evolution*

200 The understanding of the role played by SW and MS ions, solar radiation and micro-meteorites in
201 bombarding, in altering the surfaces and atmospheres of these bodies, as well as the determination
202 of the mass loss rate of the respective bodies (Killen and Ip, 1999; Madey et al. 2002) provides a
203 relevant contribution to the study of the evolution of solid bodies of the Solar System. To begin this

ambitious and challenging study, we have, as stated in §1, selected the EB in the Solar System, that are not protected by either strong magnetic fields or thick atmospheres. Such bodies are directly exposed to the incident radiations, and the resulting released atoms and molecules can escape with least hindrance. On the other hand, those atoms that fail to escape populate the surface-bound exospheres (*e.g.*, Johnson, 2002). The choice of EB also minimizes interference, such as deflection by strong local magnetic fields or/and scattering by intervening atmospheric particles, on the incident radiation as well as on the ejecta from the site of impact.

Among the processes occurring on the surfaces of EB, which include TD, PSD, IS and MIV, we select, also stated in §1, IS (ion sputtering) the first process for investigation. Our choice of IS on EB to begin our study on surface evolution is not just because we recognize the principal role of the time-varying ion flux intensity over the last 4.54 Gy in space weathering of bodies in our Solar System (Orsini et al, 2009c), but also due to the fact that three necessary sets of observables can be made accessible. These complementary observables are: the incident radiation, which has been and will continue to be monitored by planetary missions; the surface composition and mineralogy of EB, which have been and should be investigated by space-borne X-Ray, IR, neutrons, and gamma-ray spectrometers; and the ejecta of IS, which have distinct features that favor direct and precise detection and analysis, but yet to be implemented. Recently, *Kaguya* and Chandrayaan-1 spacecraft had X-Ray, IR, neutrons, gamma-ray and particle analyzers. Although *Kaguya* particle analyzers measure only ions and electrons, some of SHEA are ionized. A joint analysis of these kinds of observations could provide hints in this study. The future BepiColombo Mission, already including in its payload all these sensors and especially a dedicated SHEA detector, promises outstanding outcomes (see Section A1).

3.2 SHEA detection for observing space weathering

a) Energetically distinct

Different release processes produce particles within different energy ranges (Wurz and Lammer, 2003; Milillo et al., 2005; Leblanc and Johnson 2010). The ejected atoms and molecules, depending

230 on their velocity, can either return to the surface, become part of the atmosphere, escape the
231 gravitational field, or be photo-ionized and picked-up by planetary magnetospheres. The velocity
232 distributions are different for the relevant processes, and thus can serve as important signatures of
233 the processes involved. TD and PSD are more effective for volatiles (like H, He, Na, K, S, Ar) and
234 have typical energy below 1 eV (dashed lines in Figure 3(a), (b) refer to 2-eV-Na, that is, the escape
235 energy at Mercury), while IS and MIV are effective also for refractory species (e.g., Mg, Al, Si,
236 Ca), thus producing more energetic ejecta closer to stoichiometric composition. In contrast to the
237 MIV-released particles having a Maxwellian distribution of an expected peak corresponds to
238 ~2500–5000 K (Eichhorn, 1978) or a peak particle energy of ~0.6 eV, the high-energy tail of IS
239 ejecta, SHEA, on the other hand, can in principal have surface release energies above 10 eV
240 (Gnaser 2007; Wiens et al. 1997), more than sufficient to escape the local gravity (*e.g.*, 0.09
241 eV/nucleon for Mercury, 0.03 eV/nucleon for Moon). This means that releases from all other
242 processes can be excluded, when analyzing IS products through SHEA detection (Figure 3(c) and
243 also Figure 2). Nevertheless, the escape fraction of released particles depends on each specific case
244 (escape velocities, main release processes, surface properties, external conditions) and it is a
245 complicated quantity to estimate. Generally, one of the main processes responsible for the total
246 surface material loss rate is IS, but minor contribution can be due to radiation pressure for specific
247 species and to the other release processes, as well.
248 SHEA may also be distinguished from back-scattered atoms (BSA). This population is not a
249 negligible fraction of material leaving the surface, but definitely not of surface composition. BSA
250 are just neutralized impacting ions that are reflected back from the surface, so that their energy is
251 comparable to that of the incident ions. Back scattering is much more efficient for light species, like
252 H, so that both their flow velocity and energy are well separated from those characterizing the IS
253 ejecta, SHEA. This means that an instrument is able to discriminate between these two signals
254 provided that its ToF or energy resolution is high enough. If we consider 1 keV proton onto regolith

surface, we can assume a total yield of ion sputtering about 10%, and that of backscattering about 20%, then, the expected fluxes are comparable.

SHEA mapping on EB is distinctly different from ENA (energetic neutral atoms) imaging remote plasma such as planetary magnetospheres or moons (e.g., Hsieh & Curtis, 1988; Krimigis et al., 2004). The latter relies on the production of energetic atoms by charge-exchange between energetic ions and ambient atoms and molecules along the line of sight and within the solid angle of the ENA imager. The intensity of charge-exchange ENA flux is, therefore, a column-density measurement along the line of sight. The choice of EB as the solid target and IS as the process effectively renders any ENA produced along the line-of-sight between EB and the SHEA detector insignificant, because the charge-exchange cross section typically $< 10^{-14}$ cm^2 for ~10-eV ions (e.g., Lindsay and Stebbings, 2005), the number density of atoms in interplanetary space is $\sim 10^{-1}$ cm^{-3} (e.g., Bzowski, Fahr & Rucinski, 1996, Bzowski et al., 2008), and distance between EB surface and the observing spacecraft (s/c), hence the path length for ENA, $\sim 10^{2\text{-}3}$ km. Hence, the product of these three quantities indicates that the maximum ENA flux that can reach the observing s/c from the observed EB would be $\sim 10^{-6}$ of the ambient ion flux. This is orders of magnitude smaller than the expected SHEA flux under the bombardment of the same ion flux, due to the fact that the all-species-integrated sputtering yield is of the order 0.1, in the case of a regolith surface hit by 1-keV proton. Moreover, ion fluxes at 10 eV are usually negligible in the EB environment; generally, charge-exchange ENA are in the keV range, when the plasma is mainly SW, or they can have higher energies when considering the giant planets magnetospheres, and ion directions are generally not from the body to the s/c. So the expected ENA flux comes from different directions and at different energy range from those of SHEA.

Having distinguished SHEA from back-scattered neutrals, charge-exchange ENA and ejecta of other surface-altering processes, we arrive at the unique advantage of observing targeted EB in SHEA.

b) SHEA-mapping: instantaneous & localized

While the ground-hugging exospheres of EB maybe a mixture of lingering releases from all other surface processes over time, escaping SHEA, on the other hand, travel ballistic trajectories from their ejection sites or ion-impact site to the observing spacecraft, thus carrying instantaneous and localized information on their origins. SHEA enable us to directly map the spatial distribution of the ion impact flux in time. Correlating observed time profile of SHEA with that of the impinging ions, *e.g.* SW or MS ions, bombarding the surface, with the knowledge of surface composition provided by means mentioned in the beginning of §2, it is not difficult to imagine how the specific yield and erosion rate could be obtained, within the time-spatial and mass resolution of the SHEA instrument.

4. Necessary ground truth

In the face of the attractive and unique advantage of observing surface erosion of EB by IS *via* SHEA, we caution the need for minimizing the uncertainties from the complexity of the surface being bombarded by ions of different species and energy and ejecting SHEA of different species and energies. This prerequisite for extracting information reliably from the three sets of data – incident ion fluxes, surface composition, and SHEA maps – must be guided by solid ground truths found only in extensive laboratory data on sputtering mechanisms and yields.

Quantitative laboratory simulations and computer modeling of IS occurring on EB are essential for understanding SHEA data from planetary missions. This is analogous to the need for ground truth in remote sensing: only on-site measurements that help calibrate aerial photographs and satellite imagery can make data interpretation and analysis credible. It has been suggested that measurements of composition and kinetics of atoms and molecules in a body's exosphere during an orbiting mission could determine the importance of the different surface release mechanisms, and the surface composition (e.g., Johnson et al., 1998). In particular, the IS process will require laboratory measurements to support existent and future planetary missions. We cite here some existing use of theoretical knowledge of IS on space data (see Appendix), and where laboratory data are needed to resolve complexities that theory alone proves difficult.

306 As mentioned in §2, the ejection of surface atoms or molecules by IS is characterized by the yield *Y*.
307 At projectile energies of the order keV, *e.g.*, SW, IS occurs due to electronically-elastic knock-on
308 (ballistic) processes that are fairly well described by the linear cascade theory (Sigmund 1969). For
309 certain insulators, the electronic excitations produced by the projectile can live long enough to
310 produce what is known as electronic sputtering (Johnson, 1990). The relative importance of these
311 two processes depends on ion velocity and charge state.
312 According to the standard linear collision cascade theory, the elastic sputtering yield for atomic
313 targets is proportional to the ratio of the energy deposited at the surface and the binding energy of
314 the surface atoms. This concept has been widely used to estimate the contribution of sputtering to
315 the exosphere of Mercury, the Moon, the NEO and the Jupiter moons (Wurz and Lammer 2003;
316 Massetti et al., 2003; Leblanc et al. 2007; Mura et al., 2009, Plainaki et al., 2009, Plainaki et al.,
317 2010). Concerning this last case, the sputtering is much more complex, since electronic sputtering
318 occurs. In fact, this process is very effective in materials with low cohesive energies such as the
319 frozen gases in the outer solar system, often referred to as "ices". For such materials the total
320 electronic sputtering yield *Y* is often proportional to the square of the electronic-stopping cross
321 section. Early laboratory sputtering data by Brown et al. (1982) were used to predict the principal
322 atmospheric component of Europa, O_2, and its average column density (Johnson et al., 1982). In
323 addition, the predicted large sputtering yields have led to the suggestion that other trace species
324 should be present (Johnson et al. 1998).
325 Electronic sputtering is closely related to desorption induced by electronic transitions (DIET) (e.g.,
326 Madey et al. 2002). In DIET, an incident electron, ion or photon excites a surface state, which can
327 relax by ejecting an ion or a neutral. This is a process that is linear in the excitation cross sections
328 and is responsible for the sodium atmospheres on Mercury and the Moon (Yakshinskii and Madey
329 2000). The DIET process occurring on Mercury and the Moon is molecularly specific and is,
330 therefore, efficient for specific trace species (primarily the alakali's) or molecules adsorbed on
331 refractory surfaces. Energetic electrons, ions or photons can produce deep excitations which, in

332 principal, can result in the ejection of a large variety of surface species. However, such excitation
333 events typically occur with lower probability. The interest in knock-on sputtering is that it is more
334 robust and could eject into the gas phase species that are more representative of the surface
335 composition. With the discovery of calcium ejected from Mercury's surface, this would appear to
336 be born out. However, predictions for bodies with silicate surfaces, like the Moon (Johnson and
337 Baragiola 1991), have been much less successful than is the case for the icy bodies discussed above.
338 This fact is primarily because the yields are small (<<1 atom per ion), *e.g.*, for SW bombardment,
339 so that the sputtering of an element is more sensitive to its molecular surroundings, and, as
340 discussed below, there is insufficient data on refractory planetary materials. In attempting to model
341 this process, there are several reasons that would discourage the use of the linear cascade theory to
342 estimate the elastic sputtering yield contribution to the planetary exospheres as currently being
343 applied in atmospheric models. The theory was developed for mono-atomic targets, it assumes a
344 constant binding energy for atoms at the surface, and since it is based on a transport theory
345 approximation, it only works for amorphous materials. Of critical importance in planetary science is
346 the so-called "threshold regime", where the model breaks down and empirical models are used.
347 Sputtering becomes even more complex, if the target consists of two or more different atomic
348 species. The complication arises because the energy transfer from the projectile to the various target
349 species is different. More important, each species has a different binding energy to the lattice and,
350 therefore, irradiation leads to enhanced diffusion and depletion of the more volatile species resulting
351 in a change of the composition of the solid with depth.
352 Sputtering yields are usually measured on relatively flat laboratory surfaces. However, meteoritic
353 bombardment over millions or billions of years on the surface of an astronomical body produces a
354 regolith, a porous surface composed of grains formed by cumulative fracture and crater ejecta. Ions
355 impact a regolith structure over a range of incident angles. Since the sputtering yield depends
356 steeply on the local incidence angle θ (for ices the standard linear cascade theory predicts a
357 dependence of $\cos^{-f}\theta$, where f is between 1-2 and is nearly independent of the projectile energy;

358 Fama et al., 2008), one would expect that the yield from a regolith would be different compared to a
359 hypothetical flat surface. This effect has been evaluated using Monte Carlo simulations by Cassidy
360 and Johnson (2005), who found that the total sputtering could be significantly lower than the
361 laboratory yields.
362 In contrast with the numerous studies of the sputtering of water ice (see Baragiola et al., 2003 and
363 Famá et al., 2008 and references therein) which have been of useful application for analysis of outer
364 planetary systems (e.g., Johnson et al. 2008), there are few laboratory measurements of sputtering
365 of neutrals and secondary ions from minerals (Betz and Wehner, 1983; Jull et al. 1980; Elphic et al.
366 1991; Betz and Wien, 1994; Wiens et al. 1997). Therefore, measuring sputtering rates and velocity
367 distributions of sputtered species from minerals and ices relevant to planetary surfaces is essential to
368 support SHEA data from future planetary missions. Because such measurements are time intensive
369 and can often not be made over the full energy range required, simulations of sputtering are critical
370 for extending the range of applicability, especially in the threshold region. Both Monte Carlo test
371 particle simulations and Molecular Dynamics simulations have been carried out. The Monte Carlo
372 simulations, typically only track recoils with energies much greater than the cohesive energy of the
373 solid, and necessarily give results equivalent to those obtained from the linear Boltzmann equations.
374 The best known of such calculations are the heavily used TRIM/SRIM models (see Section 2).
375 However, these are applicable only in regions in which linear cascade model is valid and fail in the
376 threshold regime. Much more useful are the Molecular Dynamics methods which are, of course,
377 much more computationally intensive. In such models the atoms and/or molecules in the materials
378 interact with each other and with the incoming ions via intermolecular potentials. To date, they have
379 been primarily applied to model materials (Tucker et al. 2005; Bringa et al. 2000), but extensions to
380 materials with compositions and properties similar to surfaces of the Moon and Mercury are
381 feasible. Because the intermolecular potentials are not known in details for complex materials, both
382 types of simulations are typically calibrated to experiment. Therefore, they are primarily useful as
383 means for extending the range of the available data. This combination of laboratory experiments

384 and numerical simulations will be essential to support the proposed SHEA instrumentation and
385 mission design.
386
387 ## 5. Conclusion
388 In the interest of understanding what kind of evolution led to the present composition of planetary
389 atmospheres, including that of Earth, we need to learn how the current rates of the on-going
390 processes that cause surface modifications and particle escapes vary under different conditions. To
391 begin, we suggest concentrating on planets, moons and small bodies that are not protected by either
392 strong magnetic fields or thick atmospheres, *i.e.* EB (exposed bodies). Furthermore, we identified
393 IS (ion sputtering) on EB as the first process for detailed investigation for three reasons:
394 1. Incessant bombardment by either SW (solar-wind) or MS (magnetospheric) ions on the
395 respective EB constitutes predominant relevant process in altering the surface and consequently the
396 associated ground-hugging exosphere.
397 2. The ejected products of IS on the surface, SHEA (sputtered high-energy atoms), are mostly
398 neutral and energetic enough not only to be distinct from surface-released particles from other
399 processes, but also to escape local gravity and magnetic field for remote sensing.
400 3. Remote sensing in SHEA can provide mapping of the EB under IS with temporal and mass
401 resolution.
402 We illustrated what is possible and what is needed to realize remote sensing IS on EB in SHEA. In
403 the Appendix, referenced computer simulations using existing sputtering data and realistic EB
404 models are shown. We hope this paper has initiated the drive towards determining how the rates of
405 the on-going IS processes that cause the changes vary under different SW and MS conditions.
406 For such an effort, we see that parallel to planning flyby or orbiter missions to EB and developing
407 SHEA instrumentation (e.g.: BepiColombo/SERENA/ELENA Orsini et al. 2009, 2010) for such
408 missions, performing sputtering experiments in the laboratories using appropriate incident ions and
409 impacting surface analogues is equally necessary. The latter would indeed produce data crucial for

410 the planning of the missions and design of SHEA instruments as well as for extracting factual
411 information from the ensuing SHEA data.
412
413 Acknowledgements: This paper is supported by the Italian Space Agency I_081_09_0 agreement
414 for the BepiColombo/SERENA scientific activity. The comprehensiveness and quality of this paper
415 are made possible by the critical reading and advice of G. Ho, M. Hilchenbach, and S. Selci.
416

417 Appendix: Simulations

418 Based on currently available IS data and theoretical models of EB, we present here material
419 extracted from recently published papers, on what could be expected from SHEA imaging, by
420 simulation of the following EB in their particular environments: *A.1*) Mercury, when the
421 interplanetary magnetic field (IMF) configurations and SW conditions permit the plasma to reach
422 the planetary surface, *A.2*) the Moon, in the SW while outside the Earth magnetosphere, or when it
423 crosses the plasma sheet, *A.3*) asteroids and small bodies continuously exposed to the solar-wind
424 plasma, and *A.4*) the Jovian moons, Europa and Ganymede, when embedded in the Jupiter
425 magnetosphere radiation belts.

426 *A.1 Mercury*

427 SHEA measurements of Mercury should be particularly intriguing, since they would give the
428 opportunity to investigate the MS and planet interaction with the intense SW flux at about 0.3 AU.
429 Many authors (e.g., Killen et al. 2001; Sarantos et al. 2001; Kallio and Janhunen, 2003; Massetti et
430 al., 2003) showed that under specific IMF configurations, SW can enter through the cusps in the
431 dayside MS, eventually reaching the surface at mid-latitudes. Under different IMF conditions, the
432 configuration of the Hermean MS changes so that the area of high proton precipitation (hence: of
433 subsequent SHEA release) moves accordingly (e.g., Sarantos et al., 2001; Kallio and Janhunen,
434 2004; Massetti et al., 2007). Ground-based observations, indeed frequently indicate mid-latitude
435 exospheric Na densities to vary over timescales of hours (Leblanc and Johnson et al. 2010). The

436 nature of such variations is still unresolved, but it appears to be related to plasma precipitating
437 regions (Orsini et al, 2008; Mura et al. 2005; Leblanc et al., 2007; Mura et al., 2009).
438 The main constituents of the Hermean exosphere are probably volatiles released thermally or by
439 PSD. Not contained in the exosphere, but directly ejected and escaping the gravity will be the flux
440 of SHEA. The sensor ELENA (Orsini et al. 2009), part of the SERENA particle package (Orsini et
441 al. 2010) on board *BepiColombo* ESA-JAXA mission (launch 2014; Benkhoff et al., 2010) will
442 permit for the first time to map the IS emission, less intense than the PSD emission, but more
443 effective in releasing refractories from the Hermean surface (Milillo et al. 2005). The flux of ~1-5
444 keV SW protons hitting the Hermean surface is estimated $\sim 10^9$ cm^{-2} s^{-1}; a total sputtering yield
445 ~10% of the incident ion flux would lead to a total sputtered flux $\sim 10^8$ cm^{-2} s^{-1}. Approximately 50%
446 of the ejected particles escape the planet along ballistic trajectories; and ~1% of these particles have
447 enough energy (> 20 eV) to be detected by the ELENA sensor. For comparison, the back scattering
448 flux is of the same order of magnitude as that of the sputtered signal, but with an energy spectrum at
449 higher energies. The top-left panel of Figure A1 shows simulated total sputtered flux from
450 Mercury's surface over the Northern hemisphere (Mura et al., 2005). The portion of the surface
451 seen in SHEA from a vantage point at 400 km altitude, latitude 45° and LT 1200, is illustrated in
452 the lower-left panel.
453 As BepiColombo Mercury Planetary Orbiter (MPO, where SERENA will be mounted) will fly over
454 Mercury at low altitudes (orbit: 400x1550 km, see Benkhoff et al., 2010), ELENA's narrow field of
455 view (4° x 76°, with 4° x 4° resolution) will ground-track the Mercury's surface in SHEA along the
456 MPO orbital path, as shown in the upper-right panel of Figure A1. The lower right panel puts a
457 single scan in perspective to the SHEA emitting region shown in the lower left panel.
458 Eventually, SHEA imaging by ELENA will map the proton precipitation regions, with the help of
459 the simultaneous detection of the back-scattered neutrals, with surface spatial resolution between 15
460 and 50 km, depending on s/c altitude. Simulations show that ELENA's spatial and time resolution
461 capability will allow monitoring the dynamical behaviour of the magnetospheric configuration;

462 whereas its spatial resolution of tens km will allow to discriminate surface emissivity variations: as
463 explained in §4, the intensity of the directional SHEA signal depends on both ion precipitation flux
464 and surface properties, like composition and intrinsic sputtering yield.

465 *A.2. The Moon*

466 The relative importance of IS as a source process for the lunar exosphere remains questionable,
467 despite the extensive telescopic observations of Na on the Moon. This is due to the limitations of
468 the viewing geometry from Earth. The Na emission clearly decreases when the Moon lies inside the
469 terrestrial magnetosphere as would be consistent with a substantial reduction of ion precipitation
470 contribution to this process (e.g., Potter and Morgan, 1994), but this decrease coincides with a
471 changing line of sight: the observer at or close to full Moon is limited to observing the terminator
472 limb, where flux-dependent sources are weak. As a result, interpretation of the existing ground-
473 based data must necessarily rely on transport models, which account for this geometrical effect.
474 Solar-wind proton sputtering of Na (Figure A2) is suggested to be unimportant under the
475 assumption of yields $0.01 - 0.1$ per ion, contributing ~ 1 % of the total sodium exosphere. Based on
476 the yields for desorption induced by electronic transition processes that are measured in laboratory
477 studies (e.g., Madey et al., 1998; 2002), PSD is the dominant sodium source process, while
478 vaporization of regolith material caused by MIV has been suggested to constitute up to 50 % of the
479 local density of sodium at the terminator, although models may disagree (e.g., Leblanc and Johnson
480 2010). For refractory species, which remain undetected as neutrals, yet have been identified as
481 pickup ions (Mall et al., 1998; Yokota et al., 2009), impact vaporization is expected to be the
482 dominant source process, although ejection in the form of molecular oxides and their subsequent
483 photo-dissociation remains a candidate (Morgan and Killen, 1997). However, considerable
484 uncertainties still exist regarding both the flux of micrometeoroids at 1 AU (Cintala, 1992; Love
485 and Brownlee, 1993) and the effect of multiply-charged solar wind heavy ions, which are common
486 during Coronal Mass Ejection (CME) events. *In-situ* SHEA measurements are needed to constrain
487 the sputtering source. Furthermore, the detection of asymmetries in back-scattered fluxes linked to

488 magnetic anomalies (observed by Wieser et al., 2010) allows remote sensing of the effects of SW
489 interaction with the micro-magnetospheres due to local magnetism. Simultaneous observation of IS
490 emission in SHEA would add necessary details on surface-SW interaction.
491 The sputtered density of the major species of the lunar regolith (O, Al, Si, Mg, ...) is shown in Fig
492 A2(b). Sputter yields and elemental abundances consistent with Wurz et al. (2007) were assumed.
493 At 50-km where a possible orbiter could be located, all the IS species (mainly O and Si) have
494 densities of the order of 4 cm^{-3} in agreement with the estimation of Milillo et al. (2010). This flux
495 might increase following the exposure of the lunar surface to Earth's plasma sheet ions, which
496 impart approximately three times higher energy than SW ions. Measured enhancements of the
497 sodium exosphere at full Moon have been correlated to such plasma sheet crossings (Wilson et al.,
498 2006; Sarantos et al., 2008).

499 *A3. Asteroids and small bodies*

500 Asteroids suffer erosion and surface alteration from SW and solar and galactic cosmic-ray
501 bombardment, as well as from solar-photon irradiation and micrometeorites gardening.
502 Consequently, the relevant surface release processes, when they are within few AU from the Sun,
503 are IS, PSD and MIV. TD is strongly temperature dependent; hence, its contribution to exosphere
504 generation becomes important only at about 1 AU from the Sun, and increases when moving
505 towards perihelion. The detection and analysis of SHEA from asteroids separates IS from the
506 contribution from other release processes, thus SHEA detection would enable speculating on the
507 surface erosion under different environmental conditions. SW sputtering investigation provides
508 important clues on the evolution of a planetary body.
509 Solar-wind precipitation on the surface of an asteroid can be strongly influenced by the presence of
510 magnetic fields. This seems to be the case of Vesta; in fact, Vernazza et al. (2006) identified a lower
511 limit of 3 10^{16} A m^2 for eventual possible Vesta magnetic dipole, capable to deviate the solar wind
512 away from its surface. Not only a dipole can deviate SW from hitting the surface of an asteroid, but
513 also smaller magnetic structures, known as mini-magnetospheres (Winglee et al., 2000), similarly to

514 what has been imaged at the Moon in back-scattered neutral atoms, showing a reduction of neutral
515 flux from the surface corresponding to a strong magnetic anomaly (Wieser et al., 2010). The
516 possible presence of such magnetic structures can cause a reduction of the SHEA flux released from
517 an asteroid, thus minimizing local erosion and surface alteration effects.

518 A study on asteroids' exosphere based on the simulation of the various release processes on the
519 surface of the body has been performed by Schläppi et al. (2008), for the asteroids (2867) Steins
520 and (21) Lutetia, in preparation of the Rosetta flybys. They found SW sputtering to be the most
521 important exospheric supply process on the sunlit side of an asteroid. At the near Earth distances, IS
522 is expected to be even more significant.

523 The escape velocity of a Near Earth Object (NEO) is very low (i.e. 0.52 m/s for a NEO of mass
524 $\sim 10^{12}$ kg and of radius ~0.5 km), the particles released from the surface of a NEO are, therefore,
525 essentially lost in space. Given a specific model for the simulation of the various release processes
526 happening on the surface of a NEO, the efficiency of each of the particle-release processes can be
527 estimated. Clearly, identifying the NEO surface properties and its interactions with SW can provide
528 important information on the effects of space weathering on localized surface regions as well as the
529 global evolution history of the body.

530 Plainaki et al., (2009) applied the Monte Carlo SPAce Weathering on NEOs (SPAWN) model to
531 obtain the sputtered distribution around a NEO as a result of its exposure to SW (Figure A3). They
532 found that significant sputtered fluxes could reach a maximum value of 10^{11} particles m^{-2} s^{-1} around
533 the NEO. The major component of sputtered species is expected to be H. The simulated density,
534 produced by all species of sputtered particles emerging from a NEO surface, is calculated to be ~3
535 $\cdot 10^6$ particles m^{-3} near the NEO surface. The expected SHEA (E > 10 eV) fraction results in ~1% of
536 the total released particles. On the other hand, the contribution to the total density of the volatiles
537 emerging from the NEO surface, via the PSD process, is ~ $1 \cdot 10^8$ particles/m^3.

538 The global analysis of the sputtering erosion of the NEO surface would provide unique information
539 about the present and the past of the NEO's surface, revealing the mechanism through which the
540 solar wind has interacted with the surface atoms, in the past millions of years.

541 *A4. Europa and other Jovian moons*

542 The radiation environment of Europa consists of intense H^+, O^+, S^+, and C^+ ion fluxes, in the energy
543 range from keV to MeV (peaking at ~100 keV). These ions can erode the surface of Europa via ion
544 sputtering, ejecting up to 1000 H_2O molecules per incident ion, and also break the chemical bonds
545 of the ejected species resulting in the formation of new molecules (e.g. O_2), a process called
546 radiolysis. The neutrals produced have a characteristic spectrum (Cooper et al. 2001; Strazzulla *et*
547 *al.*, 2003; Paranicas *et al.*, 2002). Plainaki et al. (2010) found that the most significant sputtered-
548 H_2O emerging flux and density come from impinging S^+ ions, and they amount to 66% and 59% of
549 the total ($3.2 \cdot 10^{13}$ H_2O m^{-2} s^{-1} and $2.7 \cdot 10^{10}$ H_2O $/m^3$, respectively). The total sputtering rate for
550 Europa was calculated to be ~ 10^{27} H_2O/s with escaping ratio 22%. This value, locally on the
551 moon's surface, may exhibit variations; probably, it is higher in the trailing face, where the
552 precipitation is foreseen to be more intense. In fact, this result is inside the range for the Europa loss
553 rate given in literature and ranging between a few 10^{26} H_2O s^{-1} and 10^{28} H_2O s^{-1} (Lanzerotti et al.,
554 1982; Johnson et al., 1981; Eviatar et al., 1981, 1985; Shi et al., 1995; Ip, 1996). A similar result is
555 also derived by the Energetic Particle Detector (EPD) data on the Galileo mission, $1.1 \cdot 10^{26}$ atoms/s
556 (Ip et al., 1998).

557 Estimated energy spectra for IS, PSD, and ion backscattering (IBS) processes on Europa are shown
558 in Figure A4 (Plainaki et al., 2010). Clearly, IS is far more productive, hence, SHEA dominates
559 over releases from IBS (mainly H) and PSD at energies < 1 keV.

560 The slightly lower incident ion fluxes and the similarity between Ganymede and Europa in surface
561 composition, drives the conclusion that slightly less SHEA fluxes are expected at Ganymede, where
562 the internal magnetic field is not able to shield the plasma (Kivelson et al. 2002). Callisto, on the
563 other hand, is considerably out of Jupiter's radiation belt; hence, the expected SHEA flux should be

564 considerably lower in nominal conditions. A comparative detection of SHEA from these three
565 Jovian moons would be of particular interest in the study of Jupiter system's evolution.
566 At Mercury, 1-keV solar wind H-ions release various types of atoms (like Na, Ca, K, Mg), and
567 probably some molecules, too. Binding energies of these species with the surface of the planet are
568 between 1 and few eVs. At the Galilean moons, 100-keV H, O and S ions of Jupiter's
569 magnetospheric plasma, release mainly H_2O. The sputtered particle energy distributions for
570 molecular ices tend to have maxima at lower energies of about 0.05 eV (Boring et al. 1984, Haring
571 et al., 1984). Simulations of ion sputtering show that at Europa and Mercury in the precipitation
572 areas, the fluxes of the released particles differ at about one order of magnitude (10^9 particles/cm^2/s
573 at Europa (Plainaki et al., 2010) and 10^8 particles/cm^2/s at Mercury (Mura et al., 2005)). However,
574 according to Cassidy and Johnson (2005), in the non-ice regions of Europa, the regolith can
575 significantly modify the relative populations of atmospheric species and their spatial distributions
576 across the surface. Consequently, the sputtering yields should be reduced due to sticking of
577 sputtered species to neighboring grains (Hapke, 1986; Johnson, 1989) and therefore lower fluxes of
578 sputtered particles would be expected.
579 Estimated escape fractions of sputtered particles from the different environments and the rough
580 fraction of exposed bodies surfaces considered in this review are summarized in Table 1.
581

582 ## References

583 Baragiola, R. A., Vidal, R. A., Svendsen, W., Schou, J., Shi, M., Bahr, D. A., Atteberry, C. L.,
584 Sputtering of water ice, *Nucl. Instrum. Methods Phys. Res. B* 209, 294, 2003
585 Bhardwaj, A., S. Barabash, Y. Futaana,Y. Kazama, K. Asamura, R. Sridharan, M. Holmström, P.
586 Wurz, and R. Lundin (2005), Low energy neutral atom imaging on the Moon with the SARA
587 instrument aboard Chandrayaan-1 mission, *J. Earth Syst. Sci.*, 114(6), 749–760,
588 doi:10.1007/BF02715960.

589 Benkhoff, J., J. van Casteren, H. Hayakawa, M. Fujimoto, H. Laakso, M. Novara, P. Ferri, H. R.
590 Middleton, R. Ziethe, BepiColombo—Comprehensive exploration of Mercury: Mission
591 overview and science goals, *Planet. Space Sci.* 58, 2-20, 2010
592 Betz, G. and Wehner, in *Sputtering by Particle Bombardment II*, Eds. R. Behrisch, Springer, Berlin
593 1983
594 Betz, G., and K. Wien, Energy and angular distributions of sputtered particles, *Int. J. of Mass*
595 *Spectrometry and Ion Processes* 140, 1–110, 1994
596 Boring, J.W., Garrett, J.W., Cummings, T.A., Johnson, R.E., Brown, W.L., 1984. *Sputtering of*
597 *solid SO_2*. Nucl. Instrum. Methods B 1, 321–326.
598 Bringa, E. M., Jakas, M., and Johnson, R. E., Spike models for sputtering: effect of the surface and the
599 material stiffness, *Nucl. Instrum. Methods Phys. Res. B* 164-165, 762, 2000
600 Brown, W.L., Augustyniak, W.M., Simmons, E., Marcantonio, K.J., Lanzerotti, L.J., Johnson, R.E.,
601 Boring, J.W., Reimann, C.T., Foti, G., Pirronello, V., Erosion and molecule formation in
602 condensed gas films by electronic energy loss of fast ions, *Nucl. Instrum. Methods* 198 (1) 1-
603 8, 1982
604 Bzowski, M., Fahr, H.J., Rucinski, D., Interplanetary Neutral Particle Fluxes Influencing the Earth's
605 Atmosphere and the Terrestrial Environment, *Icarus* 124 (1) 209-219, 1996
606 Bzowski, M., Möbius, E., Tarnopolski, S., Izmodenov, V., Gloeckler, G., Density of neutral
607 interstellar hydrogen at the termination shock from Ulysses pickup ion observations, *Astron.*
608 *Astrophys.* 491(1) 7-19, 2008
609 Cassidy, T. A., and Johnson, R. E., Monte Carlo model of sputtering and other ejection processes
610 within a regolith, *Icarus* 176, 499, 2005
611 Cassidy, T.A., R.E. Johnson, and O.J. Tucker, Trace constituents of Europa's atmosphere,
612 *Icarus* 201, 182-190, 2009
613 Cintala, M.J., Impact-induced thermal effects in the lunar and Mercurian regoliths, *J. Geophys. Res.*
614 97, 947-973, 1992

615 Cooper, J.F., Johnson, R.E., Mauk, B.H., Garrett, H.B. and Neil G., Energetic ion and electron
616 irradiation of the icy Galilean Satellites, *Icarus* 149, 133-159, 2001
617 Eichhorn, G., Heating and vaporization during hypervelocity particle impact, *Planet. Space Sci.* 26,
618 463-467, 1978
619 Elphic, R.C., Funsten, H.O.,III, Barraclough,,B.L., McComas, D.J., Paffett, M.T., Vaniman, D.T.,
620 Heiken, G., Lunar surface composition and solar wind-induced secondary ion mass
621 spectrometry, *Geophys. Res. Lett.* 18, 2165-2168, 1991
622 Eviatar, A., Bar-Nun, A., Podolak, M.: European surface phenomena, Icarus, 61, 185-191, 1985.
623 Eviatar, A., Siscoe, G.L., Johnson, T.V., Matson, D.L., Effects of Io ejecta on Europa. *Icarus* 47,
624 75–83, 1981
625 Famá, M., Shi, J., Baragiola, R. A., Sputtering of water ice by low energy ions, *Surface Sci.* 602,
626 156, 2008
627 Goehlich, A., Niemöller, N., Döbele, H.F., Anisotropy effects in physical sputtering investigated by
628 laser-induced fluorescence spectroscopy, *Phys. Rev. B* 62, 9349–9358, 2000
629 Goettel, K. A., Present bounds on the bulk composition of Mercury: Implications for planetary
630 formation processes, in *Mercury*, eds. F. Vilas, C. R. Chapman, and M. S. Matthews, pp. 613–
631 621, Univ. of Ariz. Press, Tucson 1988
632 Gnaser, H. Energy and angular distributions of sputtered species, in *Sputttering by Particle*
633 *Bombardments*, eds. R Behrisch and W Eckstein, pp. 231-328, Springer, Berlin 2007
634 Hapke, B. 1986. *On the sputter alteration of regoliths of outer solar system bodies*. Icarus 66, 270-
635 279.
636 Hapke, B. 2001. *Space weathering from Mercury to the asteroid belt.* J. Geophys. Res. 106, 10,039-
637 10,073.
638 Haring, R.A., Pedrys, R., Oostra, D.J., Haring, A., de Vries, A.E., 1984. Reactive sputtering of
639 simple condensed gases by keV ions. III. Kinetic energy distributions. Nucl. Instr. Methods B
640 5, 483–488.

641 Hofer, W.O., Angular, energy, and mass distribution of sputtered particles. in *Sputtering by Particle*
642 *Bombardment*, Eds. R. Behrisch and K. Wittmaack, pp. 15–90, Springer, Berlin 1991
643 Hsieh, K.C., Curtis, C.C., A model for the spatial and energy distributions of energetic neutral
644 atoms produced within the Saturn/Titan plasma system, *Geophys. Res. Lett.* 15, 772-775, 1988
645 Ip, W.H., Europa's oxygen exosphere and its magnetospheric interaction, *Icarus* 120, 317-325,
646 1996
647 Ip, W.-H., Williams, D. J., McEntire, R.W. and B.H. Mauk: Ion sputtering and surface erosion at
648 Europa, *Geophys. Res. Lett.* 25, 829-832, 1998
649 Johnson, R.E., 1989. Application of laboratory data to the sputtering of a planetary regolith, Icarus,
650 78, 206-210.
651 Johnson, R.E., *Energetic Charged-particle Interactions with Atmospheres and Surfaces*, Springer,
652 Berlin 1990
653 Johnson, R.E., and R. Baragiola, Lunar surface: sputtering and secondary ion mass spectrometry.
654 *Geophys. Res. Lett.* 18, 2169-2172, 1991.
655 Johnson, R.E., Lanzerotti, L.J. Brown, W.L., and T.P.Armstrong, Erosion of Galilean satellite
656 surfaces by Jovian magnetosphere particles, *Science*, 212, 1027-1030, 1981
657 Johnson, R.E., Surface Boundary Layer Atmospheres, in *Atmospheres in the Solar System:*
658 *Comparative Aeronomy, Geophysical Monograph* 130, 203- 219, 2002.
659 Johnson, R. E., Lanzerotti L. J., Brown, W. L., Planetary applications of ion-induced erosion of
660 condensed-gas frost, *Nucl. Instrum. Methods*, 198, 147, 1982
661 Johnson, R. E., Killen, R. M., Waite, J. H., and Lewis, W. S., Europa's Surface composition and
662 Sputter- Produced Ionosphere, *Geophys. Res. Letts.* 25, 3257, 1998
663 Johnson, R.E, Famá, M., Liu, M., Baragiola, R.A., Sittler Jr., E.C., Smith, H.T., Sputtering of ice
664 grains and icy satellites in Saturn's inner magnetosphere, *Planet. Space Sci.* 56, 1238, 2008
665 Johnson, R.E., R.W. Carlson, T.A. Cassidy, M Famá, in *Sputtering of Ices in The Solar System Ices*,
666 Eds. M. Gutipati, in press 2010

667 Jull, A. J. T., Wilson, G. C., Long, J. V. P., Reed, S. J. B., Pillinger, C. T., Sputtering Rates of
668 Minerals and Implications for Abundances of Solar Elements in Lunar Samples, *Nucl.*
669 *Instrum. Methods*, 168, 357, 1980
670 Kallio, E., and P. Janhunen, Modelling the solar wind interaction with Mercury by a quasineutral
671 hybrid model, *Annal. Geophysic.* 21 (11) 2133-2145, 2003
672 Kallio, E., and P. Janhunen, The response of the Hermean magnetosphere to the interplanetary
673 magnetic field, *Adv. Space Res.*, 33 (12) 2176-2181, 2004
674 Killen, R.M., Ip, W-H., The surface-bounded atmospheres of Mercury and the Moon,
675 *Rev. Geophys.*, 37 (3) 361-406, 1999
676 Killen, R., G. Cremonese, H. Lammer, S. Orsini, A. E. Potter, A. L. Sprague, P. Wurz, M. L.
677 Khodachenko, H. I. M. Lichtenegger, A. Milillo and A. Mura, Processes that promote and
678 deplete the Exosphere of Mercury, Space Science Reviews 132, 433-509, 2007
679 Killen, R.M., Potter, A.E., Reiff, P., Sarantos, M., Jackson, B.V., Hick, P., Giles, B., Evidence for
680 space weather at Mercury. *J. Geophys. Res.* 106, 20509–20525, 2001
681 Kivelson, M.G., et al., The permanent and inductive magnetic moments of Ganymede, *Icarus*
682 157(2), 507–522, 2002
683 Krimigis, S. M., Mitchell, D. G., Hamilton, D. C., Livi, S., Dandouras, J., Jaskulek, S., Armstron, T.
684 P., Boldt, J. D., Cheng, A. F., Gloeckler, G., Hayes, J. R., Hsieh, K. C., Ip, W.-H., Keath, E.
685 P., Kirsch, E., Krupp, N., Lanzerotti, L. J., Lundgren, R., mauk, B. H., McEntire, R. W.,
686 Roelof, E. C., Schlemm, C. E., Tossman, B. E., Wilken, D., Williams, D. J., "Magnetosphere
687 Imaging Instrument (MIMI) on the Cassini Mission to Saturn/Titan", *Space Sci. Rev*, 114 (1)
688 233-329 (2004).
689 Lammer, H., Wurz, P., Patel, M.R., Killen, R., Kolb, C., Massetti, S., Orsini, S., Milillo, A., The
690 variability of Mercury's exosphere by particle and radiation induced surface release process.
691 *Icarus* 166, 238–247, 2003.

692 Lanzerotti, L.J., Brown, W.L., Augustyniak, W.M., Johnson, R.E., and T.P. Armstrong: Laboratory
693 studies for charged particle erosion of SO_2 ice and applications to the frosts of Io, *Astrophys.*
694 *J.* 259, 920-929, 1982.
695 Leblanc, F, and R.E. Johnson Mercury Exospheric Global Circulation Model: I, The sodium
696 Component, *Icarus*, 2010
697 Leblanc, F., Chassefière, E., Johnson, R. E., Hunten, D. M., Kallio, E., Delcourt, D. C., Killen, R.
698 M., Luhmann, J. G., Potter, A. E., Jambon, A., *et al.*, Mercury's exosphere origins and
699 relations to its magnetosphere and surface, *Planet. Space Sci.* 55, 1069, 2007
700 Lindsay, B.G. and Stebbings, R.F., Charge transfer cross sections for energetic neutral atom data
701 analysis, *J. Geophys. Res.*110 (A12) 12213, 2005
702 Love, S.G., Brownlee, D.E., A direct measurement of the terrestrial mass accretion rate of cosmic
703 dust, *Science* 262 (5133) 550, 1993
704 Madey, T.E., Yakshinskiy, B.V., Ageev, V.N., Johnson, R.E., Desorption of alkali atoms and ions
705 from oxide surfaces - Relevance to origins of NA and K in atmospheres of Mercury and the
706 moon, *J. Geophys. Res.* 103, 5873, 1998
707 Madey, T. E., Johnson R. E., and Orlando, T. M., Far-out surface science: radiation-induced surface
708 processes in the Solar System, *Surface Sci.* 500, 838, 2002
709 Mall, U., Kirsch, E., Cierpka, K., Wilken, B., Söding, A., Neubauer, F., Gloeckler, G., Galvin, A.,
710 Direct observation of lunar pick-up ions near the Moon, *Geophys. Res. Lett.*, 25 (20), 3799-
711 3802, 1998
712 Massetti, S., Orsini, S., Milillo, A., Mura, A., De Angelis, E., Lammer, H., and Wurz, P., Mapping
713 of the cusp plasma precipitation on the surface of Mercury, *Icarus* 166, 229, 2003
714 Massetti, S., Orsini, S., Milillo, A., Mura, Modelling Mercury's magnetosphere and plasma entry
715 through the dayside magnetopause, *Planet. & Space Sci.* 55, 1557-1568, 2007
716 McComas, D. J., Allegrini, F., Bochsler, P., Frisch, P., Funsten, H. O., Gruntman, M., Janzen, P. H.,
717 Kucharek, H., Möbius, E., Reisenfeld, D. B., Schwadron, N. A., Lunar backscatter and

718 neutralization of the solar wind: First observations of neutral atoms from the Moon, *Geophys.*
719 *Res. Lett.* 36 (12) L12104, 2009
720 Milillo, A., Wurz, P., Orsini, S., Delcourt, D., Kallio, E., Killen, R. M., Lammer, H., Massetti, S.
721 Mura, A., Barabash, S., Cremonese, G., Daglis, I. A., De Angelis, E., Di Lellis, A. M., Livi,
722 S., Surface-exosphere-magnetosphere system of Mercury, *Space Sci. Rev.*, 117, 397–443,
723 2005
724 Milillo, A., V. Mangano, A. Mura, S. Orsini, E. De Angelis, A. M. Di Lellis, S. Massetti, C.
725 Plainaki, R. Rispoli, S. Selci, N. Vertolli, Exosphere generation of the Moon investigated
726 through a high energy neutral detector, *Exp Astron,* in press, doi: 10.1007/s10686-010-9196-z,
727 2010
728 Morgan, T.H., Killen, R.M., A non-stoichiometric model of the composition of the atmospheres of
729 Mercury and the Moon, *Planet. & Space Sci.* 45, 81-94, 1997
730 Mura, A., S. Orsini, A. Milillo, D. Delcourt, S. Massetti. Dayside H^+ circulation at Mercury and
731 neutral particle emission. *Icarus*, 175, 305–319, 2005
732 Mura, A., Milillo, A., Orsini, S., Massetti, S., Numerical and analytical model of Mercury's
733 exosphere: Dependence on surface and external conditions, *Planet. Space Sci.* 55, 1569-1583,
734 2007
735 Mura, A., P. Wurz, H.I.M. Lichtenegger, H. Schleicher, H. Lammer, D. Delcourt, A. Milillo, S.
736 Massetti, M.L. Khodachenko, S. Orsini, The sodium exosphere of Mercury: Comparison
737 between observations during Mercury's transit and model results, *Icarus*, 200, 1-11, 2009.
738 Orsini, S., L.G. Blomberg, D. Delcourt, R. Grard, S. Massetti, K. Seki, J. Slavin, Magnetosphere-
739 exosphere-surface coupling at Mercury, SSR, DOI 10.1007/s11214-007-9221-3, 2007 and
740 Space Sciences Series of ISSI, Mercury, 26, , 2008
741 Orsini, S.; Mura, A.; Milillo, A.; Mangano, V.; Plainaki, C.; de Angelis, E.; Massetti, S.; Rinaldi,
742 G.; Rispoli, R., The Influence of Space Environment on the Evolution of Mercury, American
743 Geophysical Union, Fall Meeting 2009, abstract #P21A-1203, 2009a.

744 Orsini, S., A.M. Di Lellis, A. Milillo, E. De Angelis, A. Mura, S. Selci, I. Dandouras, P. Cerulli-
745 Irelli, R. Leoni, V. Mangano, S. Massetti, F. Mattioli, R. Orfei, C. Austin, J-L Medale, N.
746 Vertolli, D. Di Giulio, *Low energy high angular resolution neutral atom detection by means*
747 *of micro-shuttering techniques: the BepiColombo SERENA/ELENA sensor*, proceeding of the
748 conference "*Future perspective of space plasma and instrumentation and international*
749 *collaboration*", Rikkyo University, Tokyo, Japan, (1-3 November 2006), Eds. M. Hirahara, I.
750 Shinohara, Y. Miyoshi, N. Terada, T. Mukai, AIP 1144, 91, 2009b
751 Orsini, S., A. Mura, A. Milillo, V. Mangano, C. Plainaki, E. De Angelis, S. Massetti, G. Rinaldi, R.
752 Rispoli, The Influence of Space Environment on the Evolution of Mercury, *Eos Trans. AGU,*
753 *90(52), Fall Meet. Suppl.*, Abstract P21A-1203, 2009c
754 Orsini, S., S. Livi, K. Torkar, S. Barabash, A. Milillo, P. Wurz, A. M. Di Lellis, E. Kallio and the
755 SERENA team, SERENA: a suite of four instruments (ELENA, STROFIO, PICAM and
756 MIPA) on board BepiColombo-MPO for particle detection in the Hermean environment,
757 *Planet. & Space Sci*, 58, 166-181, 2010
758 Paranicas, C, Ratliff, J.M., Mauk, B H., Cohen, C. and Johnson, R.E The ion environment near
759 Europa and its role in surface energetics, *Geophys. Res. Letters*, 29 (5) 1074, 2002
760 Plainaki, C., A. Milillo, S. Orsini, A. Mura, E. De Angelis, A. M. Di Lellis, E. Dotto, S. Livi, V.
761 Mangano, S. Massetti, M. E. Palumbo, Space Weathering on Near Earth Objects based on
762 neutral particle detection, *Planet. Space Sci.* 57, 384–392, 2009
763 Plainaki, C., A. Milillo, A. Mura, S. Orsini and T. Cassidy, Neutral particle release from Europa's
764 surface, *Icarus*, 210, 385–395, 2010.
765 Potter, A.E., Morgan, T.H., Variation of lunar sodium emission intensity with phase angle,
766 *Geophys. Res. Lett.* 21, 2263-2266, 1994
767 Saito, Y., S. Yokota, T. Tanaka, K. Asamura, M. N. Nishino, M. Fujimoto, H. Tsunakawa, H.
768 Shibuya, M. Matsushima, H. Shimizu, F. Takahashi, T. Mukai, and T. Terasawa, Solar wind

769 proton reflection at the lunar surface: Low energy ion measurement by MAP-PACE onboard
770 SELENE (KAGUYA), *Geophys. Res. Letters*, 35, L24205, 2008
771 Sarantos, M., Reiff, P.H., Hill, T.H., Killen, R.M., Urquhart, A.L., A Bx-interconnected
772 magnetosphere model for Mercury. *Planet. Space Sci.*. 49, 1629–1635, 2001
773 Sarantos, M., Killen, R.M., Slavin, J.A., The effect of solar wind impact on the lunar sodium
774 emission, American Geophysical Union, Spring Meeting 2008, abstract #P34A-03, 2008.
775 Schläppi, B., K. Altwegg, and P. Wurz, Asteroid Exosphere: A Simulation for the ROSETTA flyby
776 targets (2867) Steins and (21) Lutetia, *Icarus*, 195, 674–685, 2008
777 Shi, M., Baragiola, R.A., Grosjean, D.E., Johnosn, R.E., Jurac, S. and Schou, J.: Sputtering of water
778 ice surfaces and the production of extended neutral atmospheres, *J. Geophys. Res.*, 100 (E12)
779 26387-26395, 1995
780 Sieveka, E. M., and R. E. Johnson, Ejection of atoms and molecules from Io by plasma-ion impact,
781 *Astrophys. J.* 287, 418–426. 1984
782 Sigmund, P., Theory of sputtering. I. Sputtering yield of amorphous and polycrystalline targets,
783 *Phys. Rev.* 184, 383, 1969
784 Sigmund, P., Theoretical aspects of atomic mixing by ion beams, *Nucl. Instrum. Methods*, 182-183,
785 25-41, 1981
786 Strazzulla G., Leto G., Gomis O., Satorre M.A.: Implantation of carbon and nitrogen ions in water
787 ice, *Icarus* 164, 163, 2003
788 Tucker, O. J., Ivanov, D. S., Johnson, R. E., Zhigilei, L. V., and Bringa, E. M., Molecular dynamics
789 simulation of sputtering from a cylindrical track: EAM versus pair potentials, *Nucl. Instrum.*
790 *Methods B* 228, 163, 2005
791 Vernazza, P.; Brunetto, R.; Strazzulla, G.; Fulchignoni, M.; Rochette, P.; Meyer-Vernet, N.;
792 Zouganelis, I., Asteroid colors: a novel tool for magnetic field detection? The case of Vesta,
793 *Astron. & Astrophys.* 451 (3) L43-L46, 2006

794 Wiens, R.C., D.S. Burnett, W. F. Calaway, C. S. Hansen,2 K. R. Lykke,3 and M. J. Pellin, Sputtering
795 Products of Sodium Sulfate: Implications for Io's Surface and for Sodium-Bearing Molecules in
796 the Io Torus, *Icarus* 128, 386–397, 1997
797 Wieser, M., Barabash, S., Futaana, Y., Holmström, M., Bhardwaj, A., Sridharan, R., Dhanya, M.B.,
798 Wurz, P., Schaufelberger, A. and Asamura, K., Extremely high reflection of solar wind
799 protons as neutral hydrogen atoms from regolith in space, *Planet. Space Sci.,* 57, 2132–2134,
800 2009
801 Wieser, M., S. Barabash, Y. Futaana, M. Holmström,1 A. Bhardwaj, R. Sridharan, M. B. Dhanya, A.
802 Schaufelberger, P. Wurz and K. Asamura, First observation of a mini magnetosphere above a
803 lunar magnetic anomaly using energetic neutral atoms, *Geophys. Res. Letters*, 37, L05103, 2010
804 Wilson, J.K., Mendillo, M.; Spence, H.E., Magnetospheric influence on the Moon's exosphere,
805 *J. Geophys. Res*. 111 (A7) CiteID A07207, 2006
806 Winglee, R. M.; Slough, J.; Ziemba, T.; Goodson, A., Mini-Magnetospheric Plasma Propulsion:
807 Tapping the energy of the solar wind for spacecraft propulsion, *J. Geophys. Res*. 105 (A9)
808 21067-21078, 2000
809 Wurz, P., and Lammer, H., Monte-Carlo simulation of Mercury's exosphere, *Icarus*, 164, 1, 2003
810 Wurz, P., Rohner, U., Whitby, J. A., Kolb. C., Lammer, H., Ddobnikar, P., Martín-Fernández, The
811 lunar exosphere: the sputtering contribution, *Icarus* 191, 486, 2007
812 Yakshinskiy, B.V., Madey, T.E., Desorption induced by electronic transitions of Na from SiO_2:
813 relevance to tenuous planetary atmospheres, *Surface Sci.*, 451, 160-165, 2000
814 Yokota, S.; Saito, Y., Asamura, K., Tanaka, T., Nishino, M.N., Tsunakawa, H., Shibuya, H.,
815 Matsushima, M., Shimizu, H., Takahashi, F., Fujimoto, M.; Mukai, T., Terasawa, T., First
816 direct detection of ions originating from the Moon by MAP-PACE IMA onboard SELENE
817 (KAGUYA), DOI:10.1029/2009GL038185, 2009.
818 Ziegler J.F., Biersack J.P., Littmark U., *The Stopping and Range of Ions in Solids*, Section 6,
819 Pergamon Press, New York, 1966

820 Zurbuchen, T.H., Raines, J.M., Gloeckler, G., Krimigis, S.M., Slavin, J.A., Koehn, P.L., Killen,
821 R.M., Sprague, A.L.,McNutt, R.L., Jr., Solomon, S.C., MESSENGER observations of the
822 composition of Mercury's ionized exosphere and plasma environment, *Science* 321, (5885) 90
823 – 92, 2008
824

825 Table 1. Sputtered escape fraction from reference EB

EB	Exposed surface %	Escaping sputtered fraction %
Mercury	25	70
Moon (out of Earth's magnetosphere)	50	90
NEO	50	100
Europa	100	22

826

827 Figure 1. Examples of ion-induced SHEA ejection. Incident energetic ions are in blue and atoms of
828 the exposed surface are in red. Ejections shown are by (a) primary or first recoil, (b) knock-on by a
829 backscattered ion without a cascade, (c) secondary recoil, (d) higher order recoil or cascade, (e)
830 backscattered incident ion, and (f) backscattered recoil atom. Panels (e) and (f) are for surfaces
831 having more than one element, *e.g.*, more massive atoms (in black). The angles shown in (c) define
832 the directions of the incident ion, the recoil atom and the ejected SHEA. Panels (b) and (e) are
833 indistinguishable externally, except in the energy of the SHEA. This figure is based on Figure 2.1
834 of Sigmund (1981) and Figure 2.6 of Hofer (1991).

835 Figure 2. Some measured and computed SHEA spectra. a) Computed energy distribution function
836 $f_{S,n}$ (Eq. (2)) of Na sputtered from 1-keV protons impacting on a simulated planetary-like mineral
837 surface for different assumed Na binding energies. b) Computed $f_{S,n}$ of Na ejecta, assuming a 2 eV
838 binding energy, for protons of different energies impacting on regolith-like simulated (again
839 regolith means the porosity was account for). c) Comparison of high-energy part of Na ejecta
840 distribution (dashed line) and SRIM simulations (solid line, for the assumed surface composition
841 see Goettel, 1988) for E_i = 1 keV. d) SHEA energy spectra for Ar^+ of different E_i on W at zero
842 incident and ejection angles (Goelhich *et al.* 2000). e) Ejection of Na from Na_2SO_4 for impacting
843 Ar^+ of 3.5 keV and with $E_b \sim 0.27$eV (Wiens *et al.* 1997). f) Sputtering of D_2O ice with ~ 30% SO_2
844 bombarded by 5-keV Ar^+. Energy profile of sputtered SO_2 (red dots) and D_2O (blue dots)
845 molecules, normalized at 1 meV flux. The energy profiles are fit to two distributions of the form
846 $E_b/(E_e+E_b)^2$. The fit shows for DO_2 (blue, lower curve), U ~ 0.048 eV for a fraction 0.32 of the
847 molecules ejected with U ~ 0.0033eV for the remainder; for the SO_2 component (red, curve over the

848 dots), U ~ 0.043eV for a fraction 0.36 of the ejected molecules, with U ~ 0.0053 for the remainder
849 (Johnson *et al.* 2010).
850 Figure 3. Model of velocity distribution functions for TD (a), PSD (b) and IS (c) (adapted fm.:
851 Killen et al., 2007). See also Fig.2 for SHEA spectra. Dashed lines correspond to the Na escape
852 energy at Mercury equal to 2 eV, for reference.
853 Figure A1. Top-left panel: Pseudo-color map of SHEA flux from the Northern surface of Mercury
854 due to proton sputtering (from Mura et al., 2005). The oval-shaped dotted line is the horizon as seen
855 from the s/c (400 km above surface level); bottom-left panel: SHEA signal as seen from the s/c;
856 bottom-right panel: ELENA FoV and count-rate (color) superimposed to the SHEA signal (gray);
857 top-right panel: thanks to the s/c motion, the ground-track of ELENA data allows global imaging of
858 the surface SHEA emission.
859 Figure A2. Model of the equatorial lunar exosphere: (a) sodium density and its variation with solar
860 zenith angle, χ, and altitude for PSD, MIV, and IS; (b,c) sub-solar point profiles attributed to IS and
861 MIV for a number of other abundant lunar constituents ~~[From Sarantos et al., 2009].~~
862 Figure A3. Simulated integral flux (log(particles m^{-2} s^{-1})) of total sputtered particles from CI
863 chondrites NEO for impinging protons of energy ~1 keV. Axial symmetry is assumed; positive Y
864 points to the Sun. (Plainaki et al., 2009).
865 Figure A4. Intensity versus energy spectrum of the sputtered, back-scattered and PSD-ed neutrals at
866 Europa (Plainaki et al., 2010)
867
868

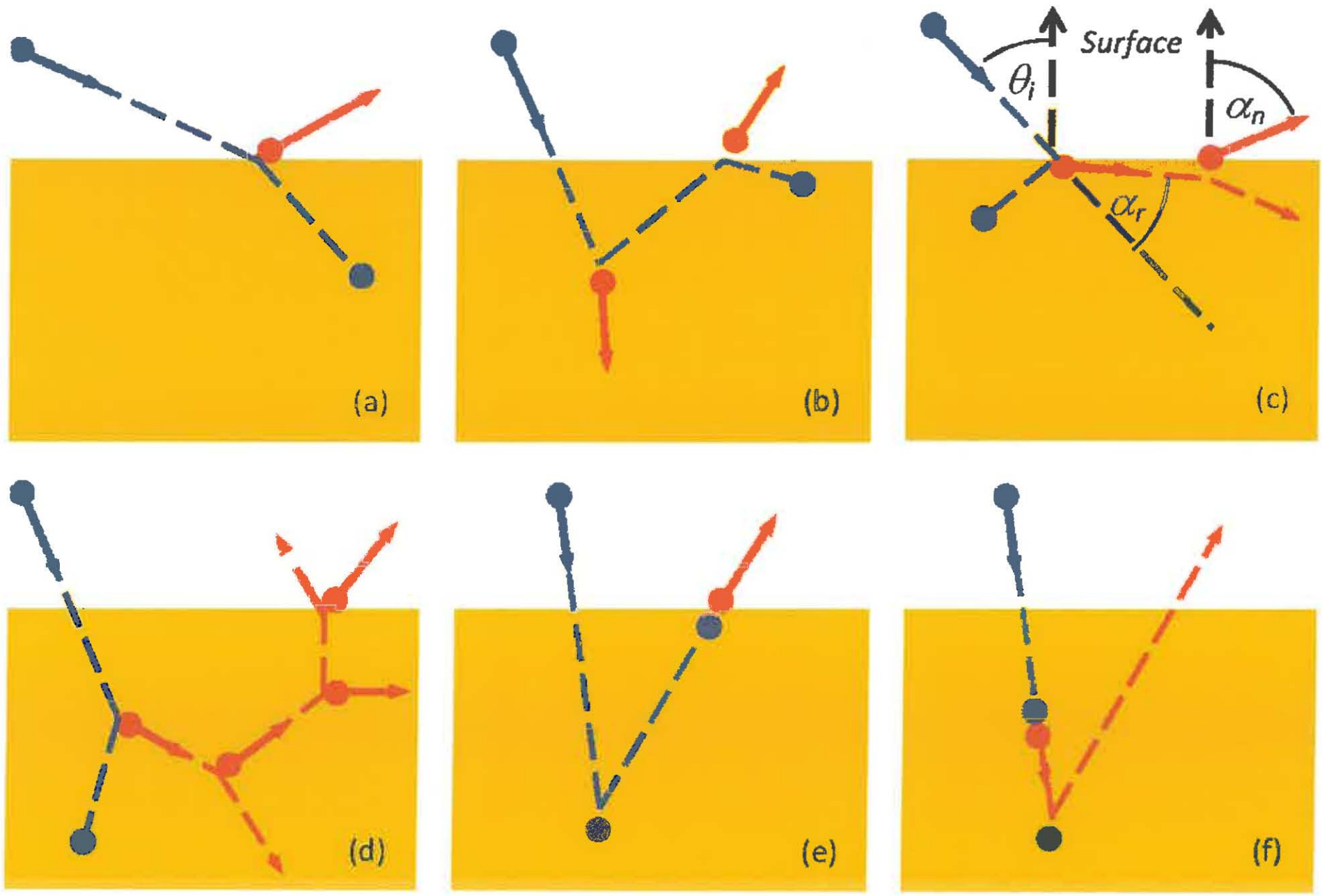
(a)
(b)
Surface
θ_i
α_n
α_r
(c)
(d)
(e)
(f)

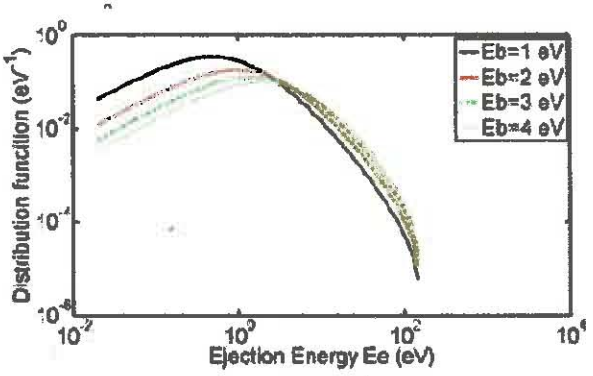
Eb=1 eV
Eb=2 eV
Eb=3 eV
Eb=4 eV
Distribution function (eV⁻¹)
Ejection Energy Ee (eV)

a)

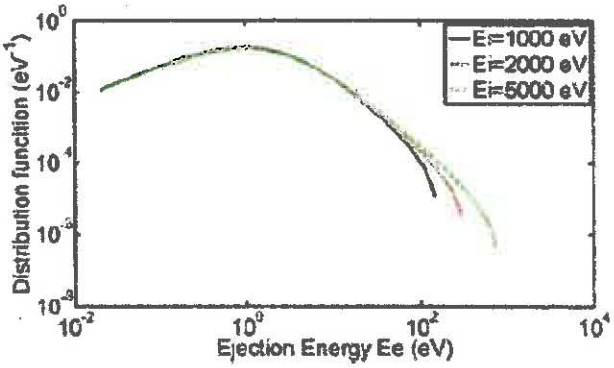
Ei=1000 eV
Ei=2000 eV
Ei=5000 eV
Distribution function (eV⁻¹)
Ejection Energy Ee (eV)

b)

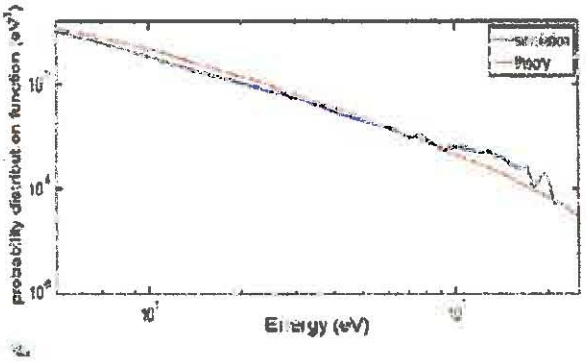
Simulation
Theory
probability distribution function (eV⁻¹)
Energy (eV)

c)

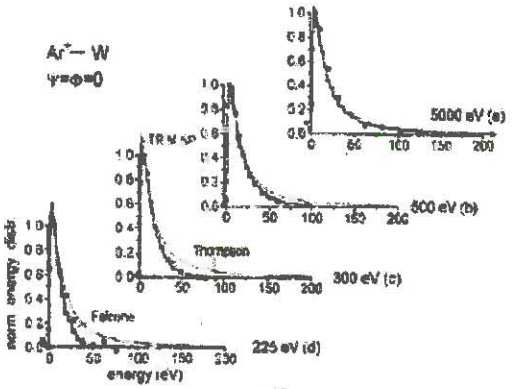
Ar⁺ — W
γ=Φ=0
5000 eV (a)
500 eV (b)
300 eV (c)
225 eV (d)
Thompson
Falcone
energy (eV)

d)

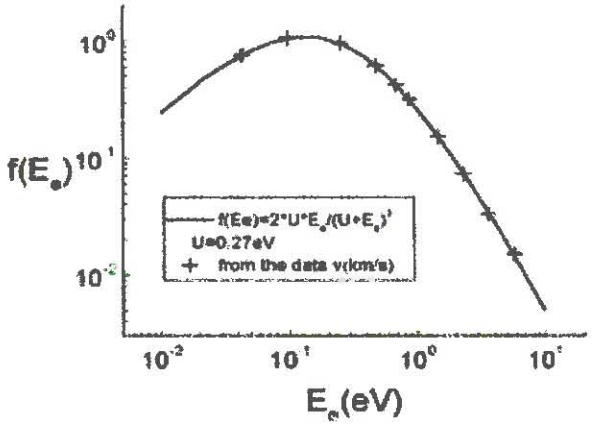
f(Ee)=2*U*Ee/(U+Ee)³
U=0.27eV
from the data v(km/s)
f(Ee)
Ee(eV)

e)

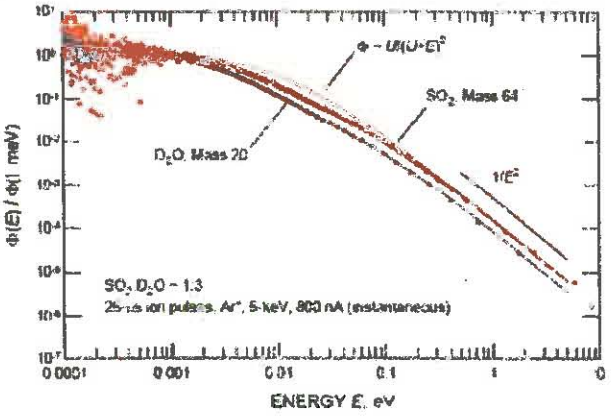
Φ ~ U/(U+E)³
SO2, Mass 64
D2O, Mass 20
1/E²
SO2, D2O ~ 1.3
25-us ion pulses, Ar⁺, 5-keV, 800 nA (instantaneous)
Φ(E) / Φ(1 meV)
ENERGY E, eV

f)

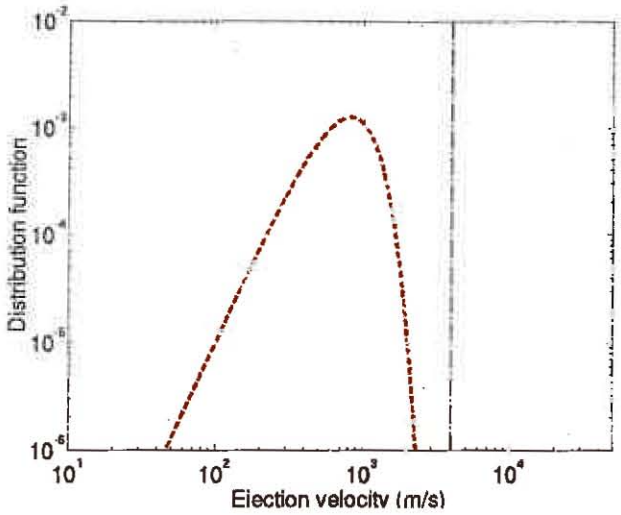
Distribution function
Ejection velocity (m/s)

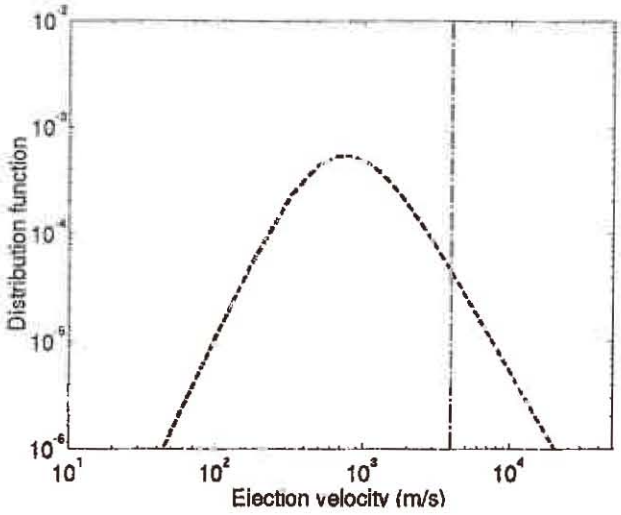
Distribution function
Ejection velocity (m/s)

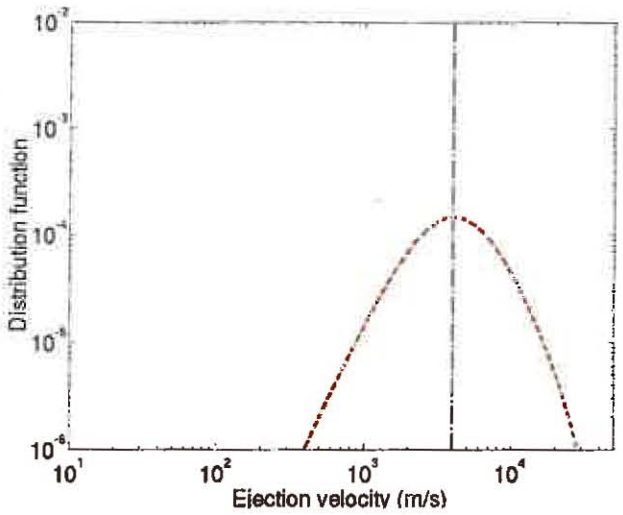
Distribution function
Ejection velocity (m/s)

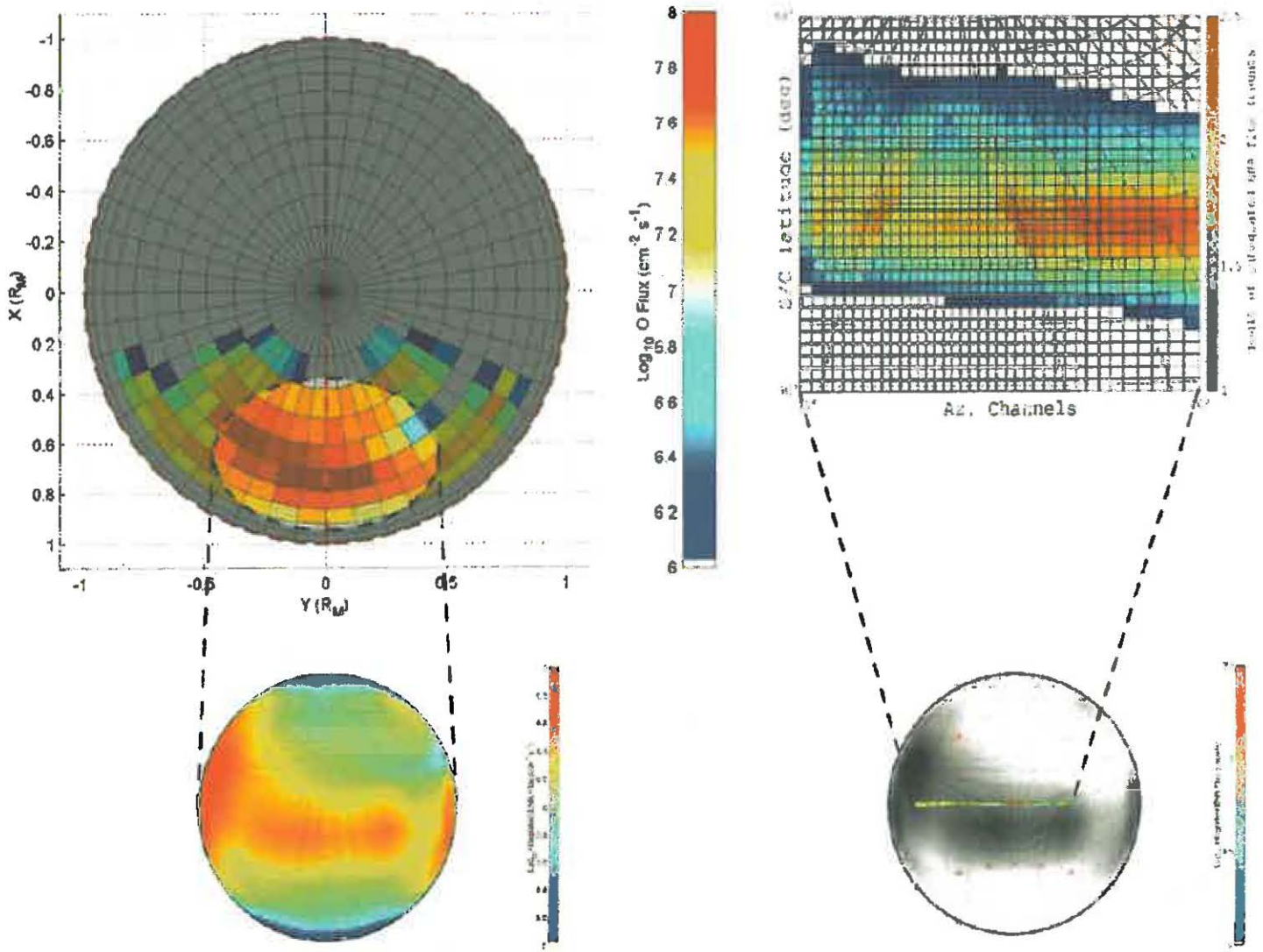
X (R_M)
Y (R_M)
Log_{10} O Flux ($cm^{-2}s^{-1}$)
Az. Channels

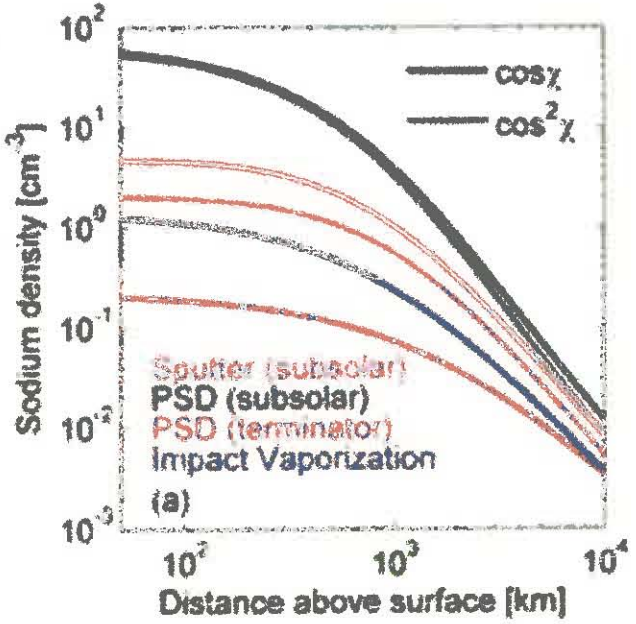
Sodium density [cm^{-3}]
Distance above surface [km]
cosχ
cos^{2}χ
Sputter (subsolar)
PSD (subsolar)
PSD (terminator)
Impact Vaporization
(a)

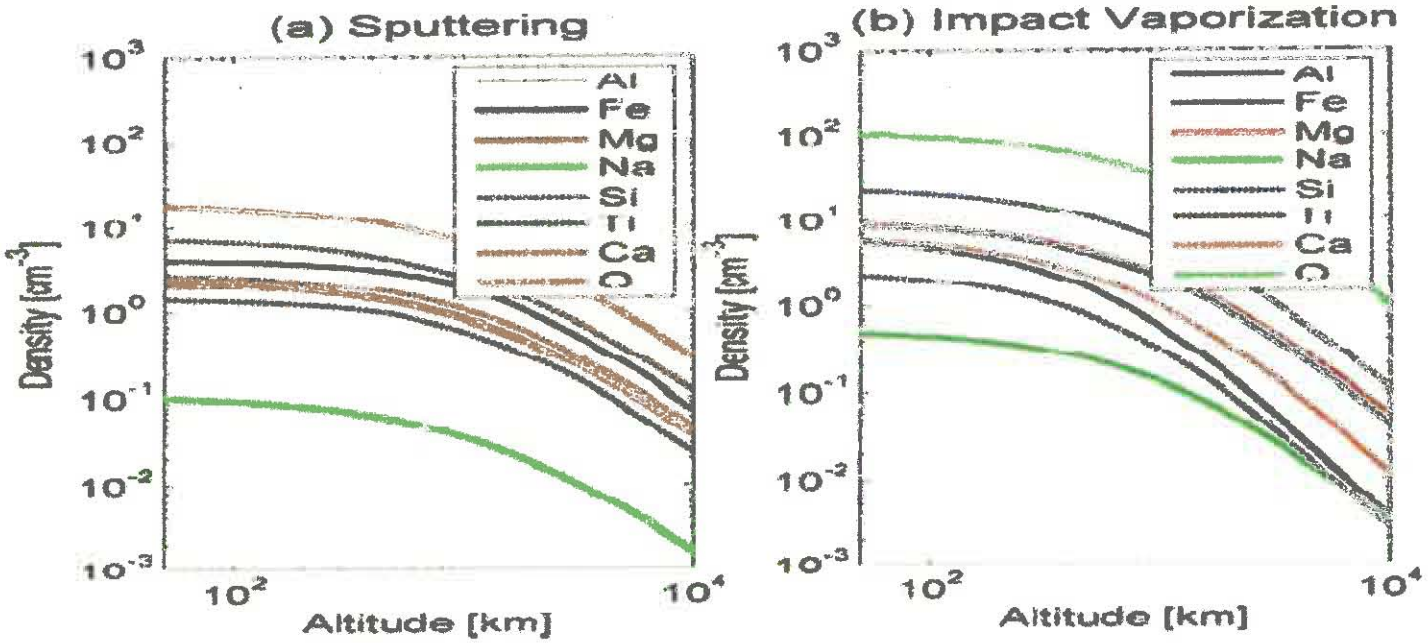
(a) Sputtering
(b) Impact Vaporization
Density [cm^{-3}]
Altitude [km]
Al
Fe
Mg
Na
Si
Ti
Ca
O

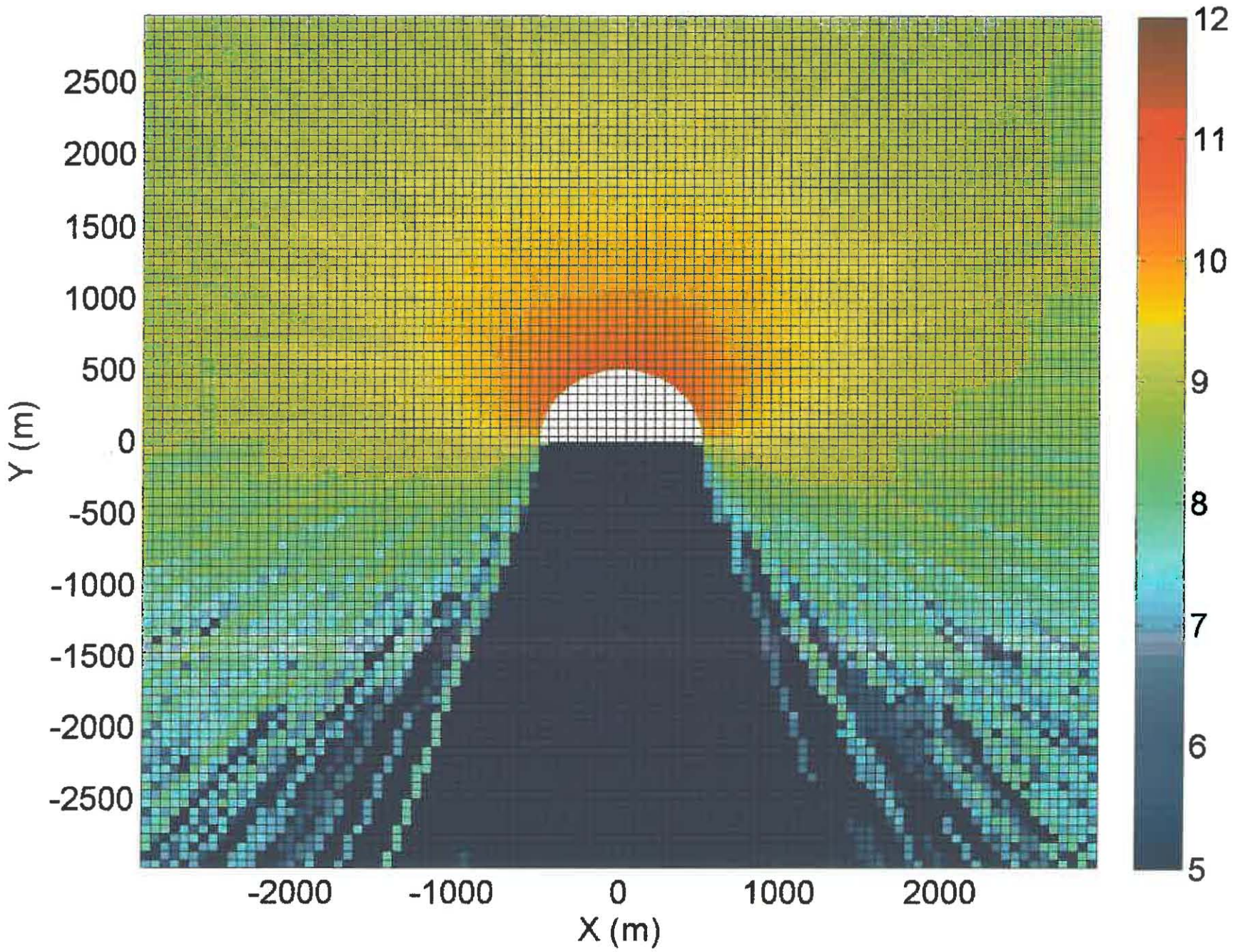
2500
2000
1500
1000
500
0
-500
-1000
-1500
-2000
-2500
Y (m)
-2000
-1000
0
1000
2000
X (m)
12
11
10
9
8
7
6
5

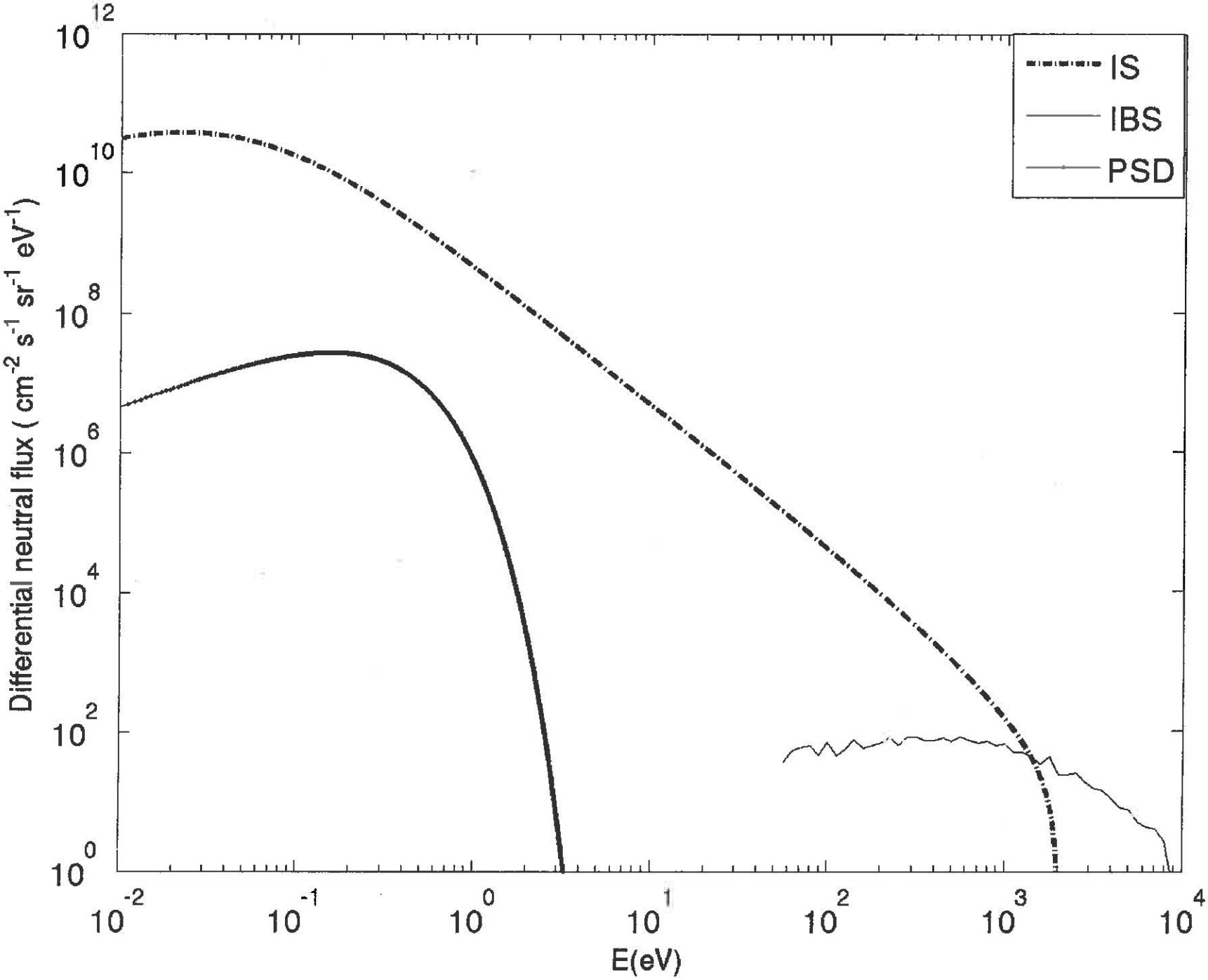
IS
IBS
PSD
Differential neutral flux (cm-2 s-1 sr-1 eV-1)
E(eV)
10^12
10^10
10^8
10^6
10^4
10^2
10^0
10^-2
10^-1
10^0
10^1
10^2
10^3
10^4